

Rethinking Implicit Spatial Representation in Visuomotor Policy Learning

Xiangyu Chen¹, Yuxuan Hu¹, Chuhao Zhou¹, Jianfei Yang^{1,†}

¹MARS Lab, Nanyang Technological University, [†]Corresponding Author

Generative model-based imitation learning has become a widely adopted paradigm for robotic manipulation, where policy performance depends critically on the conditioned visual representations. Although spatial softmax-based representations have been adopted in prior visuomotor policies, their effectiveness and underlying mechanisms remain insufficiently understood. This work rethinks the use of spatial softmax pooling: do such implicit spatial representations provide effective and stable visual features for robotic manipulation? Through systematic studies of different pooling methods in visual encoders, we find that this pooling operation produces compact and stable spatial representations, which outperform feature-value representations, despite using substantially fewer dimensions. Complementary saliency analysis further suggests that these spatial representations guide the encoder to focus more consistently on task-relevant regions. However, this advantage is limited by a representation bottleneck in current visual encoders: repeated downsampling operations weaken fine-grained spatial information before the action-generation module can use it, especially under low-resolution observations. Motivated by these findings, we propose PRISM, a visual encoder that preserves multiscale implicit spatial information through top-down cross-attention fusion. Experiments across multiple tasks and policy backbones show consistent improvements. In particular, on the low-resolution, high-precision *ToolHang* task, PRISM shows clear gains, improving the average success rate from 5.0% to 13.4% while increasing parameters by only 15.4%. These results support the use of multiscale implicit spatial representations as an effective and efficient design principle for robotic manipulation.

Correspondence: jianfei.yang@ntu.edu.sg.



1 Introduction

Imitation learning (Osa et al., 2018) has become a widely adopted paradigm for robotic manipulation, enabling robots to acquire complex manipulation skills directly from human demonstrations. Recent generative model-based policies (Chi et al., 2025; Zhan et al., 2026) have demonstrated strong generalization capability by denoising Gaussian noise into action distributions conditioned on visual features. These approaches capture multimodal behaviors and show stronger robustness, substantially advancing robotic manipulation.

Visual representation is therefore central to the generative model-based policies. Most existing policies adopt standard visual encoders, such as ResNet backbones (He et al., 2016), to extract compact representations from images. These encoders largely inherit design choices from semantic recognition, where repeated spatial downsampling and global aggregation are effective for capturing object categories and appearance cues. As a result, the learned representation tends to emphasize what visual patterns are present, rather than preserving where they occur and how they are spatially arranged (Tomasini et al., 2023).

Unlike semantic vision tasks, manipulation requires precise spatial cues for action prediction, including object pose, contact structure, and robot-object alignment. Spatial representations therefore provide a natural alternative to globally aggregated semantic feature representations, as they expose relative position information to visuomotor policies. Although spatial softmax pooling (SSPool) (Finn et al., 2016) has been adopted in prior visuomotor policies (Chi et al., 2025; Mandlkar et al., 2022), it is often treated as an architectural component rather than as a representation mechanism. Its role and effectiveness remain underexplored. Thus, our work rethinks the use of SSPool and begins with the question: **Do implicit spatial representations provide effective and stable visual features for robotic manipulation?**

We answer this question through controlled pooling ablations across three generative policy backbones, varying only what representations are extracted from the final feature maps. The results show that implicit spatial representations from SSPool consistently improve policy performance with substantially fewer feature dimensions. Saliency analysis further suggests that these spatial representations provide effective and stable visual conditioning for robotic manipulation.

Beyond the choice of representation, we further identify *spatial information collapse* as an overlooked encoder-level bottleneck in visuomotor policy design. Although standard visual encoders, such as ResNet-style backbones, are commonly adopted as default feature extractors, repeated downsampling and global aggregation can produce overly coarse final feature maps, weakening the fine-grained spatial structure needed for precise pose estimation and tool-object alignment. While high-resolution images or additional camera views can alleviate this issue, they increase system complexity without directly addressing the bottleneck inside the encoder.

Motivated by these findings, we propose *PRISM*, a visual encoder that preserves multiscale implicit spatial representations for robotic manipulation. Rather than extracting implicit spatial representations only from the final feature map, PRISM extracts coordinate-aware features from multiple residual stages and fuses them through a top-down cross-attention mechanism into a compact implicit spatial representation. This design preserves spatial cues across multiple feature resolutions, strengthens the spatial information available to the policy, and mitigates the spatial information collapse caused by aggressive encoder compression. In summary, our contributions are as follows:

- We provide empirical evidence and saliency analysis, demonstrating that implicit spatial representations are more effective and stable for robotic manipulation than globally aggregated feature-value representations, despite using substantially fewer feature dimensions.
- We identify spatial information collapse as an encoder-level bottleneck and empirically show that aggressive compression in conventional visual encoders weakens the fine-grained spatial structure required for low-resolution, geometry-sensitive manipulation.
- Motivated by this diagnosis, we propose *PRISM*, a visual encoder that extracts and fuses multiscale implicit spatial representations through multiscale spatial softmax extraction and top-down cross-attention fusion, achieving consistent improvements across manipulation tasks.

2 Related Work

Generative-Model-Based Policies Generative-model-based policies (Chi et al., 2025; Geng et al., 2026; Black et al., 2024) have become a strong paradigm for robotic manipulation. These methods denoise actions from pure noise, conditioned on visual observations and robot proprioception, making them suitable for modeling multimodal demonstrations. Recent policies predict action chunks from image observations for closed-loop manipulation (Zhao et al., 2023). While these works (Jia et al., 2026; An et al., 2026; Bai et al., 2026) improve action generation, the visual representation used to condition the policy remains critical. Most existing policies (Li et al., 2025) adopt ResNet backbones (He et al., 2016) to extract image features, although these encoders are originally developed for semantic recognition tasks such as image classification (Deng et al., 2009). This motivates our study of which visual representations provide effective and stable conditioning signals for generative visuomotor policies.

Spatial-Information-Augmented Policies Spatial information is essential for robotic manipulation, where policies infer object pose, end-effector pose, and robot-object alignment. Prior works incorporate spatial cues through coordinate-aware features (Hu et al., 2026; Ye et al., 2026), keypoints (Fang et al., 2025; Zheng et al., 2025), and object poses (An et al., 2024; Deng et al., 2025). Spatial softmax pooling (Chi et al., 2025; Finn et al., 2016; Mandlekar et al., 2022) converts convolutional feature activations into compact coordinate-like representations preserving the spatial relationship in deep features. However, its role as an implicit spatial representation mechanism remains insufficiently studied. Moreover, aggressive striding and pooling in image encoders collapse spatial information and produce coarse feature maps (Fu et al., 2024). Motivated by this gap, we systematically study implicit spatial representations for robotic manipulation and propose PRISM to preserve them across multiple feature scales.

3 Implicit Semantic vs. Implicit Spatial Representations

A visual encoder maps an input image to deep feature maps, while the representation head determines what information from these maps is exposed to the policy. Conventional heads, such as average pooling (AvgPool) and max pooling (MaxPool), aggregate feature activations into value-based descriptors that capture which visual patterns are present. In contrast, SSPool couples activations with a coordinate grid, producing coordinate-aware descriptors that capture where these patterns occur. The key distinction is therefore whether the representation only summarizes activation values or also preserves the spatial locations of feature responses. Based on this distinction, we categorize visual representations into *implicit semantic representations* and *implicit spatial representations*.

Implicit Semantic Representation. Conventional visual encoders often use global aggregation, such as AvgPool and MaxPool, to obtain compact feature representations. Given a feature map $\mathbf{F} \in \mathbb{R}^{C \times H \times W}$, these operations extract a scalar value from each channel. The resulting vector mainly reflects the presence or strength of visual features, without explicitly preserving their relative spatial locations. We therefore refer to these representations as *implicit semantic representations*.

Implicit Spatial Representation. In contrast, we refer to the output of SSPool (Finn et al., 2016; Levine et al., 2016) as *implicit spatial representations* since it combines feature activations with coordinate grids. For each channel, it normalizes activations over spatial locations and computes the expected coordinate:

$$p_{cij} = \frac{\exp(F_{cij}/\tau)}{\sum_{m=1}^H \sum_{n=1}^W \exp(F_{cmn}/\tau)}, \quad (x_c, y_c) = \sum_{i=1}^H \sum_{j=1}^W p_{cij}(x_{ij}, y_{ij}), \quad (1)$$

where τ is a temperature parameter and $(x_{ij}, y_{ij}) \in [-1, 1]^2$ denotes the normalized coordinate of location (i, j) . Unlike AvgPool and MaxPool, which summarize activation values, SSPool converts each channel into a spatial distribution and outputs the expected coordinate of the corresponding feature response. This provides coordinate-aware visual cues that are directly relevant to pose, alignment, and contact reasoning in robotic manipulation. This distinction provides the basis for our experiments, where we compare implicit semantic and implicit spatial representations.

4 Methodology

This section introduces PRISM, a visual encoding framework for preserving multiscale implicit spatial representations in robotic manipulation. While SSPool provides an effective coordinate-aware representation, applying it only to the final feature map can be limiting because current encoders repeatedly downsample visual features before pooling. This compression may weaken fine-grained spatial cues before they are exposed to the policy. To address this, PRISM extracts implicit spatial representations from different residual stages using multiscale spatial softmax (MS-SS) and aggregates these multiscale cues into a compact policy-conditioning vector through top-down cross-attention (TDCA), as shown in Fig. 1.

4.1 Multiscale Implicit Spatial Softmax

In standard ResNet-based encoders, SSPool is commonly applied only after multiple downsampling stages as the replacement of average pooling. While effective for recognition-oriented perception, this final-stage pooling can be too compressed for manipulation tasks requiring precise pose estimation, alignment, and contact reasoning. Therefore, PRISM extracts implicit spatial representations from multiple residual stages,

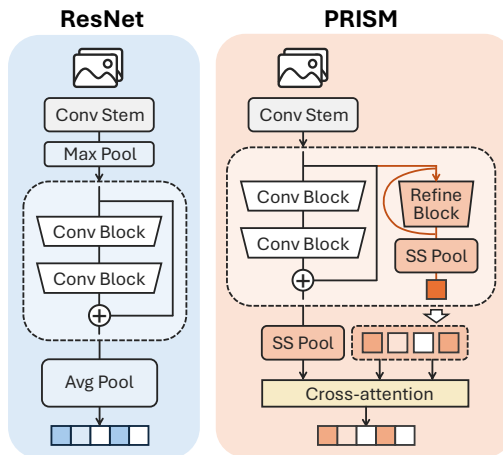


Figure 1 Overview of PRISM.

as illustrated by the right part in Fig. 1. Specifically, given the feature map \mathbf{x}^l from the l -th stage, we apply a residual refinement block before SSPool:

$$\hat{\mathbf{x}}^l = \mathbf{x}^l + \mathcal{F}_{\text{ref}}^l(\mathbf{x}^l), \quad \mathbf{s}^l = \text{SSPool}^l(\hat{\mathbf{x}}^l), \quad (2)$$

where $\mathcal{F}_{\text{ref}}^l(\cdot)$ is the refine block, $\hat{\mathbf{x}}^l$ is the refined feature map, and \mathbf{s}^l is the extracted implicit spatial representation. The multiscale spatial representations $\{\mathbf{s}^l\}_{l=1}^L$ are passed to the fusion module.

4.2 Top-Down Cross-Attention Fusion

MS-SS provides complementary multiscale implicit spatial representations. The deepest representation contains stronger task-level context due to its larger receptive field, while earlier representations retain finer spatial details with less compression. Direct concatenation combines these representations but treats all scales equally. To enable high-level context to select relevant fine-scale cues, PRISM uses a lightweight top-down cross-attention (TDCA) fusion module.

Given the multiscale spatial representations $\{\mathbf{s}^l\}_{l=1}^L$ from MS-SS module, we use the deepest spatial representation \mathbf{s}^L as the query and the earlier-stage representations $\{\mathbf{s}^l\}_{l=1}^{L-1}$ as the keys and values. For compact notation, we denote the concatenation of earlier-stage representations as $\mathbf{s}^{1:L-1} = [\mathbf{s}^1; \mathbf{s}^2; \dots; \mathbf{s}^{L-1}]$. Therefore, the TDCA is formulated as

$$\mathbf{z} = \text{softmax} \left(\frac{Q(\mathbf{s}^L)K(\mathbf{s}^{1:L-1})^\top}{\sqrt{d}} \right) V(\mathbf{s}^{1:L-1}), \quad (3)$$

where $Q(\cdot)$, $K(\cdot)$, and $V(\cdot)$ are learnable projections, and d is the attention dimension. The attended feature \mathbf{z} is then projected to a fixed-dimensional vector as the visual condition for the downstream policy. By using the deepest spatial representation as high-level context, TDCA retrieves relevant finer-scale spatial cues from earlier stages. This allows PRISM to efficiently aggregate multiscale implicit spatial representations while keeping the policy-conditioning vector compact.

5 Experimental Results

The central contribution of this work is empirical: we study whether implicit spatial representations provide effective visual features for robotic manipulation and whether PRISM can strengthen them. Our experiments are organized around five research questions:

- RQ1. What evidence supports implicit spatial representations for robotic manipulation?**
- RQ2. Does spatial compression limit geometry-sensitive manipulation?**
- RQ3. How does PRISM improve low-resolution manipulation performance?**
- RQ4. How does each component of PRISM contribute to performance?**
- RQ5. Can PRISM be deployed in multi-task and real-world scenarios?**

We answer these questions through pooling ablations, bottleneck analysis on high-precision tasks, comparisons with ResNet-based baselines, and component ablations. We further evaluate PRISM on LIBERO (Liu et al., 2023a) multi-task benchmarks to examine generalization beyond single-task settings, and include real-world experiments as physical deployment validation. All encoder comparisons use the same policy architectures, training schedules, and evaluation protocols to isolate the effect of visual representation. Detailed experimental settings are provided in Appendix A.3.

5.1 What evidence supports implicit spatial representations for robotic manipulation?

To answer this question, we isolate the effect of representation type by comparing policies with the same ResNet (He et al., 2016) encoder but different pooling strategies: average pooling (AvgPool), max pooling (MaxPool), no pooling (NoPool), and spatial softmax pooling (SSPool). While AvgPool, MaxPool, and NoPool

Table 1 Pooling ablation under standard and truncated ResNet18 backbones. Results are reported as mean success rate (%) across the three short-horizon robomimic tasks with three seeds.

Pooling	Standard ResNet18					Truncated ResNet18			
	Dim.	DP	FM	MF	Avg.	DP	FM	MF	Avg.
SSPool	64	89.7	88.7	91.6	90.0	87.3 (-2.4)	91.3 (+2.6)	90.7 (-0.9)	89.8 (-0.2)
AvgPool	512	70.9	86.0	86.4	81.1	61.6 (-9.3)	87.1 (+1.1)	84.2 (-2.2)	77.6 (-3.5)
MaxPool	512	68.4	75.1	72.2	71.9	67.1 (-1.3)	72.4 (-2.7)	66.0 (-6.2)	68.5 (-3.4)
NoPool	4608	68.2	78.2	65.8	70.7	67.1 (-1.1)	78.4 (+0.2)	73.1 (+7.3)	72.9 (+2.2)

aggregate feature activations as semantic feature-value representations, SSPool transforms feature activations into coordinate-like representations by computing channel-wise implicit spatial locations. This comparison allows us to directly examine which implicit representations provide a more effective visual conditioning signal for robotic manipulation.

We evaluate the four pooling strategies with Diffusion Policy (DP) (Chi et al., 2025; Ho et al., 2020), Flow Matching (FM) (Lipman et al., 2023), and MeanFlow (MF) (Zhan et al., 2026; Geng et al., 2026) on *Lift*, *Can*, and *Square*, as shown in the first column of Fig. 2. Given 84×84 observations, the standard ResNet18 encoder outputs a $512 \times 3 \times 3$ feature map. SSPool maps it to 64 coordinate features, whereas average and max pooling produce 512-dimensional descriptors and no pooling yields a 4608-dimensional flattened feature.

First, we visualize saliency maps for the three short-horizon tasks in Fig. 2 and Appendix A.1. Although all methods use the same ResNet as encoder, different pooling methods lead to clearly different attention patterns. SSPool produces the cleanest and most localized responses, concentrating on task-relevant regions such as the objects. In contrast, AvgPool, MaxPool, and NoPool produce more diffuse or less consistent responses. This qualitative evidence suggests that coordinate-aware SSPool helps the encoder preserve spatial cues that are useful for visuomotor control.

Second, we report the success rate under the same training setting with three seeds in Table 1. As shown in Table 1, SSPool achieves the best average success rate under the standard ResNet18 backbone, outperforming AvgPool, MaxPool, and NoPool by 8.9, 18.1, and 19.3 points, respectively, with an $8 \times$ to $72 \times$ smaller representation. The poor performance of NoPool, despite retaining the most features, shows that representation structure matters more than feature dimensionality. Together with the saliency maps, these results suggest that clean and localized spatial responses are associated with stronger robotic manipulation performance.

We further repeat the comparison with a truncated ResNet18, where the final convolutional stage is removed to reduce spatial compression. SSPool remains the best-performing strategy and is nearly unchanged on average ($90.0 \rightarrow 89.8$), whereas AvgPool and MaxPool drop by -3.5 and -3.4 points. These results suggest that SSPool provides a stable spatial representation, and that the less-compressed feature maps still contain rich implicit spatial representation. This motivates PRISM to preserve spatial representations across multiple feature scales.

To further examine whether SSPool provides structured spatial information, we conduct a channel-shuffle ablation. We randomly shuffle the K coordinate channels while preserving each (x, y) pair during training and inference. As shown in Table 2, the shuffled representation still achieves non-zero success rates, suggesting that the retained coordinates preserve useful spatial information. However, the substantial performance drop shows that the original channel organization is also important. Together, these results suggest that SSPool provides not only coordinate-level spatial cues, but also a channel-structured implicit spatial representation

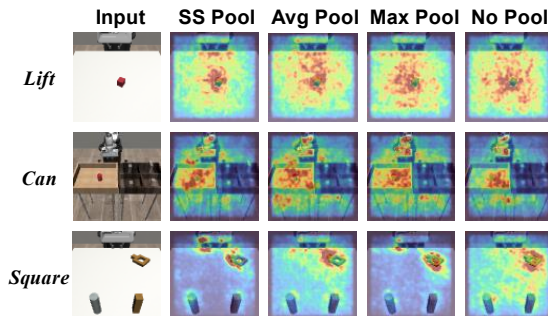


Figure 2 Saliency Maps of different pooling strategies for robomimic tasks.

Table 2 Success rates (%) of channel-shuffle ablation on SSPool.

Model	Lift	Can	Square	Avg.
DP	77±6	2±2	23±6	34.0 (-55.7)
FM	65±29	3±2	9±7	25.8 (-62.9)
MF	65±8	2±0	51±8	39.3 (-52.3)
Avg.	69.0	2.3	27.7	33.0 (-56.3)

Table 4 Robomimic PH single-task success rates (%) over three seeds (150 rollouts). PRISM is compared with the standard ResNet+SSPool baseline.

Policy	Encoder	Lift	Can	Square	ToolHang	Avg.
<i>Flow Matching</i>	Base.	99.0±1.0	90.0±3.0	77.0±4.0	4.7±1.2	67.7
	PRISM	96.7±4.6	92.7±4.6	84.7±2.3	14.0±4.0	72.0
	Gain	-2.3	+2.7	+7.7	+9.3	+4.4
<i>Diffusion</i>	Base.	97.0±2.0	96.0±2.0	76.0±6.0	5.3±2.3	67.1
	PRISM	96.7±3.1	96.7±3.1	77.3±7.0	12.7±8.1	70.9
	Gain	-0.3	+0.7	+1.3	+7.4	+3.8

for policy learning.

Overall, these results show that the advantage of SSPool comes from compact, channel-structured spatial information, rather than from higher feature dimensionality or a specific policy formulation. This motivates PRISM to preserve such spatial structure across multiple feature scales. Thus, we use the ResNet+SSPool as the baseline (Base.) in the following experiments.

5.2 Does spatial compression limit geometry-sensitive manipulation?

To answer this question, we use the *ToolHang* task with low-resolution 84×84 observations as a stress test. Unlike the short-horizon tasks in Sec. 5.1, *ToolHang* is a high-precision manipulation task that requires accurate pose estimation, tool-object alignment, and contact reasoning. As shown in Table 3, applying SSPool only to the final ResNet feature map achieves lower performance than the other pooling choices, while NoPool performs best among the baseline representations. This discrepancy with the results in Sec. 5.1 suggests a possible bottleneck: when low-resolution observations are used for geometry-sensitive manipulation, the aggressively compressed final feature map may be too coarse for SSPool to extract sufficiently fine-grained implicit spatial information.

Table 3 Pooling ablation on low-res. ToolHang.

Pooling	Dim.	SR
AvgPool	512	7.3
MaxPool	512	8.0
NoPool	4608	8.7
SSPool	64	4.7
SSPool (Trunc.)	64	7.3
MS-SSPool	384	11.3

To test this hypothesis, we provide SSPool with less-compressed and multiscale spatial features. Using TruncResNet, which removes the final convolutional stage and preserves a less-compressed feature map, improves the success rate by 55%. Moreover, multiscale SSPool improves performance by 140% and achieves the best result in this setting. These improvements support the hypothesis that aggressive encoder compression is harmful for preserving implicit spatial information in challenging manipulation tasks. Thus, the limitation comes not from implicit spatial representations themselves, but from applying spatial pooling only after visual features have already been overly compressed. This motivates PRISM to preserve implicit spatial representations across multiple feature scales.

5.3 How does PRISM improve low-resolution manipulation performance?

We compare PRISM with the ResNet+SSPool under the same policy architectures and evaluation protocol. As shown in Table 4, PRISM improves *ToolHang*, the most geometry-sensitive Robomimic task, from 4.7% to 14.0% under Flow Matching and from 5.3% to 12.7% under Diffusion Policy. Averaged across both policy backbones, PRISM improves *ToolHang* success rate from 5.0% to 13.4%, corresponding to a 168.0% relative improvement. These gains suggest that PRISM benefits difficult low-resolution manipulation while maintaining performance on simpler tasks.

These improvements are especially meaningful because *ToolHang* requires precise spatial reasoning over a long manipulation sequence, including grasping, alignment, insertion, and hanging. By extracting implicit spatial representations from multiple feature scales and aggregating them through top-down cross-attention fusion, PRISM provides the policy with richer spatial cues than final-stage SSPool. This addresses the compression bottleneck identified in Sec. 5.2 and supports the gains on geometry-sensitive manipulation.

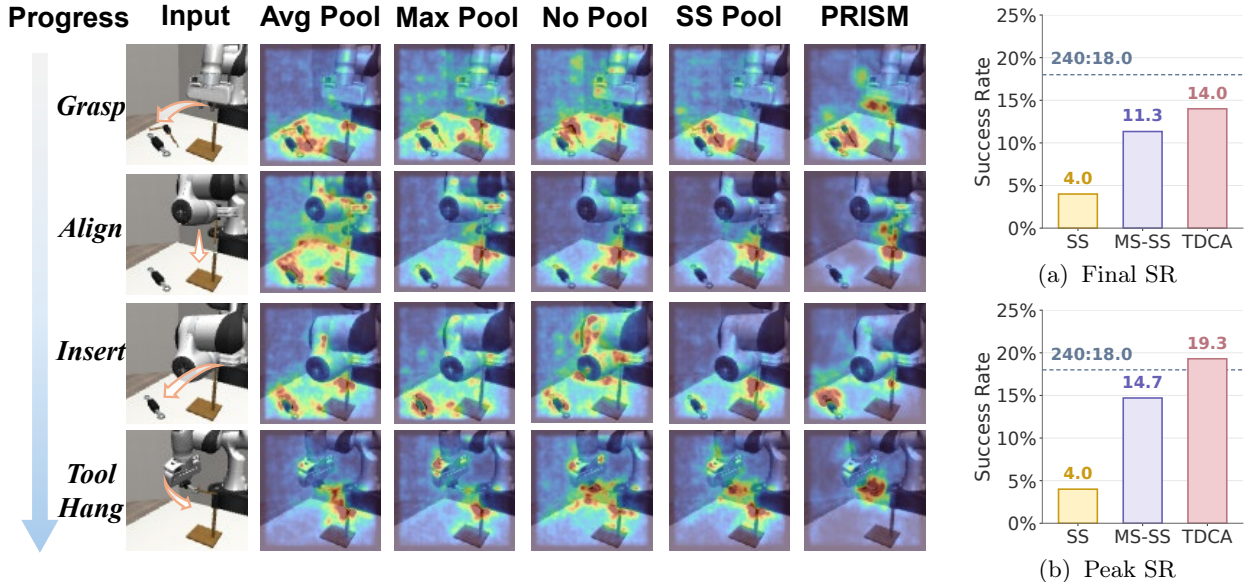


Figure 4 **Saliency maps on ToolHang.** The figures present and compare attended regions across different encoders for the key stages in the *ToolHang* task.

Figure 5 **Component ablation on ToolHang.**

We further evaluate whether this improvement extends across different input resolutions and camera views. As shown in Table 5, PRISM improves *ToolHang* performance in most settings across both 84×84 and 240×240 observations. The gains are especially clear for single-view 240×240 inputs, where PRISM improves DP, FM, and MF from 22%, 18%, and 16% to 42%, 30%, and 32%, respectively. Although not every setting improves uniformly, these results suggest that preserving multiscale implicit spatial information remains useful across different visual input configurations.

Table 5 **ToolHang success rates (%) across resolution settings (50 rollouts).**

Policy	2V-84		1V-240		2V-240	
	Base.	PRISM	Base.	PRISM	Base.	PRISM
DP	14	26	22	42	32	30
FM	16	20	18	30	26	30
MF	22	26	16	32	30	44

The saliency maps in Fig. 4 provide qualitative evidence for this improvement. Compared with the ResNet using other pooling methods, PRISM produces cleaner and more localized responses around task-relevant regions across different stages of *ToolHang*. Across grasping, alignment, insertion, and hanging, PRISM consistently attends to the robot arm, the manipulated tool, and their interaction regions. For example, during the grasp stage, PRISM focuses on both the tool and gripper, while other pooling strategies produce more diffuse or less complete responses. Together with the quantitative results, this saliency analysis suggests that preserving multiscale implicit spatial information helps the visual encoder focus on task-relevant spatial cues for high-precision manipulation.

5.4 How does each component of PRISM contribute to performance?

To answer this question, we ablate the two main components of PRISM: multiscale spatial softmax (MS-SS) and top-down cross-attention fusion (TDCA). We evaluate them on the single-view 84×84 *ToolHang* task, using 200 training epochs and 150 rollouts over three seeds. As shown in Fig. 5, MS-SS substantially improves over final-stage SSPool, indicating that preserving implicit spatial information across feature scales is important for high-precision manipulation. Adding TDCA further improves both the final and peak success rates, showing that top-down fusion helps aggregate multiscale spatial cues more effectively. Notably, the full model approaches the performance of the 240×240 reference while using only 84×84 observations, suggesting that better spatial representation can partially compensate for limited input resolution.

We further examine whether the proposed multiscale mechanism benefits other pooling methods. We evaluate multiscale variants of different pooling operators without the refining blocks on the short-horizon Robomimic tasks and report the results in Fig. 6. Multiscale SSPool achieves the highest success rate with the smallest parameter overhead, providing the best trade-off between performance and model complexity. AvgPool also

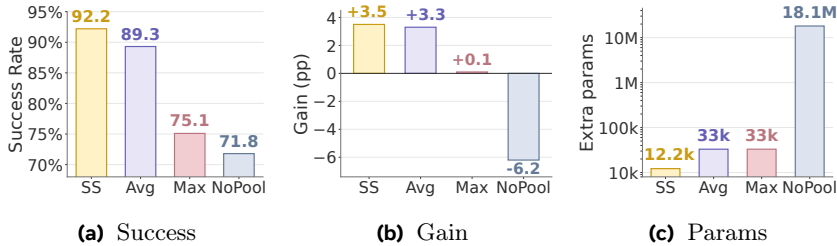


Figure 6 Effect of multiscale feature enhancement across pooling operators. The multiscale SSPool mechanism achieves the highest success rate with the lowest parameter cost.

benefits from multiscale features, but requires more additional parameters. In contrast, MaxPool yields negligible gain, and NoPool degrades performance despite a substantial parameter increase. These results suggest that multiscale features are most effective when paired with a pooling operator that preserves implicit spatial structure. We therefore use multiscale SSPool as the default spatial extraction module in PRISM.

5.5 Can PRISM be deployed in multi-task and real-world scenarios?

To answer this question, we evaluate PRISM beyond single-task Robomimic simulation. We first conduct multi-task experiments on LIBERO-10 (Liu et al., 2023a) and LIBERO-Spatial (Liu et al., 2023a) using the same FM policy as the baseline. As shown in Table 6, PRISM improves LIBERO-10 from 22.0% to 53.5% and LIBERO-Spatial from 37.0% to 52.5%. These results suggest that preserving multiscale implicit spatial representations also benefits multi-task visuomotor learning. We further conduct real-world experiments as physical deployment validation. As shown in Table 7, PRISM successfully completes the StackCube and KeyPick tasks, achieving success rates of 70.0% and 80.0%, respectively. These tasks are relatively short-horizon and less precision-demanding, which may limit the observable benefit of preserving multiscale implicit spatial representations. Nevertheless, the results show that PRISM can be deployed in physical manipulation settings without degrading performance. Details of the LIBERO dataset and real-world setup are provided in Appendix A.2.

Table 6 LIBERO results.

Encoder	10	Spatial
Base.	22.0	37.0
PRISM	53.5	52.5

Table 7 Real-world results.

Encoder	StackCube	KeyPick
Base.	70.0	80.0
PRISM	70.0	80.0

6 Limitations

Although PRISM shows consistent relative improvements across policy backbones, tasks, and input resolutions, this work has several limitations. First, PRISM introduces additional computational overhead due to multiscale spatial softmax feature extraction and top-down attention-based fusion. This overhead is more pronounced during training, since during inference visual features are extracted only once per action chunk. Second, our real-world experiments are limited in scope. They mainly serve as deployment validation on relatively simple tasks, where PRISM maintains comparable performance to the baseline but does not yet show clear gains. Future physical experiments should therefore focus on more challenging geometry-sensitive manipulation scenarios.

7 Discussion

Despite these limitations, this work provides empirical motivation for choosing implicit spatial representations in robotic manipulation. Our results suggest that coordinate-aware spatial representations can provide more effective policy inputs than compact feature-value representations. PRISM is one implementation of this principle. By preserving multiscale implicit spatial information, it addresses the spatial information loss caused by repeated downsampling in standard vision encoders. Thus, the broader contribution of this work is not only a visual encoder but also evidence that implicit spatial representations are a useful representation principle for visuomotor policy learning. We do not argue that spatial representations should totally replace semantic representations. Future work should therefore explore visual encoders that better balance semantic understanding with spatial structure, especially for contact-rich and precision-sensitive manipulation.

References

- Boshi An, Yiran Geng, Kai Chen, Xiaoqi Li, Qi Dou, and Hao Dong. Rgbmanip: Monocular image-based robotic manipulation through active object pose estimation. In *2024 IEEE International Conference on Robotics and Automation (ICRA)*, pages 7748–7755. IEEE, 2024.
- Tuo An, Jindou Jia, Gen Li, Jingliang Li, Chuha Zhou, Pengfei Liu, Bofan Lyu, Jiaqi Bai, Xinying Guo, Geng Li, et al. Feedback world model enables precise guidance of diffusion policy. *arXiv preprint arXiv:2605.15705*, 2026.
- Jiaqi Bai, Jindou Jia, Yuxuan Hu, Gen Li, Xiangyu Chen, Tuo An, Kuangji Zuo, and Jianfei Yang. Flash: Efficient visuomotor policy via sparse sampling. *arXiv preprint arXiv:2605.15492*, 2026.
- Kevin Black, Noah Brown, Danny Driess, Adnan Esmail, Michael Equi, Chelsea Finn, Niccolo Fusai, Lachy Groom, Karol Hausman, Brian Ichter, et al. π_0 : A vision-language-action flow model for general robot control. *arXiv preprint arXiv:2410.24164*, 2024.
- Cheng Chi, Zhenjia Xu, Siyuan Feng, Eric Cousineau, Yilun Du, Benjamin Burchfiel, Russ Tedrake, and Shuran Song. Diffusion policy: Visuomotor policy learning via action diffusion. *The International Journal of Robotics Research*, 44(10-11):1684–1704, 2025.
- Jia Deng, Wei Dong, Richard Socher, Li-Jia Li, Kai Li, and Li Fei-Fei. Imagenet: A large-scale hierarchical image database. In *2009 IEEE conference on computer vision and pattern recognition*, pages 248–255. Ieee, 2009.
- Shengliang Deng, Mi Yan, Songlin Wei, Haixin Ma, Yuxin Yang, Jiayi Chen, Zhiqi Zhang, Taoyu Yang, Xuheng Zhang, Heming Cui, et al. Graspvla: a grasping foundation model pre-trained on billion-scale synthetic action data. In *Conference on Robot Learning*, pages 1004–1029. PMLR, 2025.
- Xiaolin Fang, Bo-Ruei Huang, Jiayuan Mao, Jasmine Shone, Joshua B Tenenbaum, Tomás Lozano-Pérez, and Leslie Pack Kaelbling. Kalm: Keypoint abstraction using large models for object-relative imitation learning. In *2025 IEEE International Conference on Robotics and Automation (ICRA)*, pages 8307–8314. IEEE, 2025.
- Chelsea Finn, Xin Yu Tan, Yan Duan, Trevor Darrell, Sergey Levine, and Pieter Abbeel. Deep spatial autoencoders for visuomotor learning. In *2016 IEEE International Conference on Robotics and Automation (ICRA)*, pages 512–519. IEEE, 2016.
- Stephanie Fu, Mark Hamilton, Laura E Brandt, Axel Feldmann, Zhoutong Zhang, and William Freeman. Featup: A model-agnostic framework for features at any resolution. In *International Conference on Learning Representations*, volume 2024, pages 45324–45350, 2024.
- Zhengyang Geng, Mingyang Deng, Xingjian Bai, J Zico Kolter, and Kaiming He. Mean flows for one-step generative modeling. In *The Thirty-ninth Annual Conference on Neural Information Processing Systems*, 2026.
- Kaiming He, Xiangyu Zhang, Shaoqing Ren, and Jian Sun. Deep residual learning for image recognition. In *Proceedings of the IEEE conference on computer vision and pattern recognition*, pages 770–778, 2016.
- Jonathan Ho, Ajay Jain, and Pieter Abbeel. Denoising diffusion probabilistic models. *Advances in neural information processing systems*, 33:6840–6851, 2020.
- Yuxuan Hu, Xiangyu Chen, Chuha Zhou, Yuxi Liu, Gen Li, Jindou Jia, and Jianfei Yang. Trace-focused diffusion policy for multi-modal action disambiguation in long-horizon robotic manipulation. *arXiv preprint arXiv:2602.07388*, 2026.
- Jindou Jia, Gen Li, Xiangyu Chen, Tuo An, Yuxuan Hu, Jingliang Li, Xinying Guo, and Jianfei Yang. A2A: Action-to-Action Flow Matching Policy. In *Proceedings of Robotics: Science and Systems*, Sydney, Australia, July 2026.
- Sergey Levine, Chelsea Finn, Trevor Darrell, and Pieter Abbeel. End-to-end training of deep visuomotor policies. *Journal of Machine Learning Research*, 17(39):1–40, 2016.
- Jiayi Li, Yuxuan Hu, Haoran Geng, Xiangyu Chen, Chuha Zhou, Ziteng Cui, and Jianfei Yang. $\mathbf{M}^3\mathbf{A}$ policy: Mutable material manipulation augmentation policy through photometric re-rendering. *arXiv preprint arXiv:2512.01446*, 2025.
- Yaron Lipman, Ricky TQ Chen, Heli Ben-Hamu, Maximilian Nickel, and Matt Le. Flow matching for generative modeling. In *11th International Conference on Learning Representations, ICLR 2023*, 2023.

- Bo Liu, Yifeng Zhu, Chongkai Gao, Yihao Feng, Qiang Liu, Yuke Zhu, and Peter Stone. Libero: Benchmarking knowledge transfer for lifelong robot learning. *Advances in Neural Information Processing Systems*, 36:44776–44791, 2023a.
- Xingchao Liu, Chengyue Gong, and Qiang Liu. Flow straight and fast: Learning to generate and transfer data with rectified flow. In *The Eleventh International Conference on Learning Representations (ICLR)*, 2023b.
- Ajay Mandlekar, Danfei Xu, Josiah Wong, Soroush Nasiriany, Chen Wang, Rohun Kulkarni, Li Fei-Fei, Silvio Savarese, Yuke Zhu, and Roberto Martín-Martín. What matters in learning from offline human demonstrations for robot manipulation. In *Conference on Robot Learning*, pages 1678–1690. PMLR, 2022.
- Takayuki Osa, Joni Pajarinen, Gerhard Neumann, J Andrew Bagnell, Pieter Abbeel, and Jan Peters. An algorithmic perspective on imitation learning. *Foundations and Trends® in Robotics*, 7(1-2):1–179, 2018.
- Umberto M Tomasini, Leonardo Petrini, Francesco Cagnetta, and Matthieu Wyart. How deep convolutional neural networks lose spatial information with training. *Machine Learning: Science and Technology*, 4(4):045026, 2023.
- Jinhui Ye, Fangjing Wang, Ning Gao, Junqiu Yu, Zhu Yangkun, Bin Wang, Jinyu Zhang, Weiyang Jin, Yanwei Fu, Feng Zheng, Yilun Chen, and Jiangmiao Pang. Spatially guided training for vision-language-action model. In *The Fourteenth International Conference on Learning Representations*, 2026.
- Guojian Zhan, Letian Tao, Pengcheng Wang, Yixiao Wang, Yuxin Chen, Yiheng Li, Hongyang Li, Masayoshi Tomizuka, and Shengbo Eben Li. Mean flow policy with instantaneous velocity constraint for one-step action generation. In *The Fourteenth International Conference on Learning Representations*, 2026.
- Tony Z Zhao, Vikash Kumar, Sergey Levine, and Chelsea Finn. Learning fine-grained bimanual manipulation with low-cost hardware. *arXiv preprint arXiv:2304.13705*, 2023.
- Ruijie Zheng, Yongyuan Liang, Shuaiyi Huang, Jianfeng Gao, Hal Daumé III, Andrey Kolobov, Furong Huang, and Jianwei Yang. Tracevla: Visual trace prompting enhances spatial-temporal awareness for generalist robotic policies. In *International Conference on Learning Representations*, volume 2025, pages 54277–54296, 2025.

A Appendix

A.1 Additional Saliency Map Visualizations

We provide additional saliency map visualizations to qualitatively analyze how different representation heads affect the visual regions used by the policy. The saliency maps highlight image regions that have stronger influence on action prediction.

We first compare different pooling strategies on the *Lift*, *Can*, and *Square* tasks. As shown in Fig. 7, Fig. 8, and Fig. 9, SSPool-based representations tend to produce more localized and consistent saliency around task-relevant objects, the gripper, and robot-object interaction regions. In contrast, feature-value aggregation methods, such as average pooling and max pooling, often produce more diffuse or less structured saliency patterns. These qualitative results are consistent with our quantitative findings, suggesting that implicit spatial representations provide useful policy inputs by exposing where task-relevant visual features occur.

We further visualize the saliency maps of PRISM across the three tasks. As shown in Fig. 10, PRISM focuses on task-relevant regions, including the manipulated object, the gripper, and their interaction areas. This suggests that preserving multiscale implicit spatial information helps the policy maintain attention on spatially meaningful cues for manipulation.

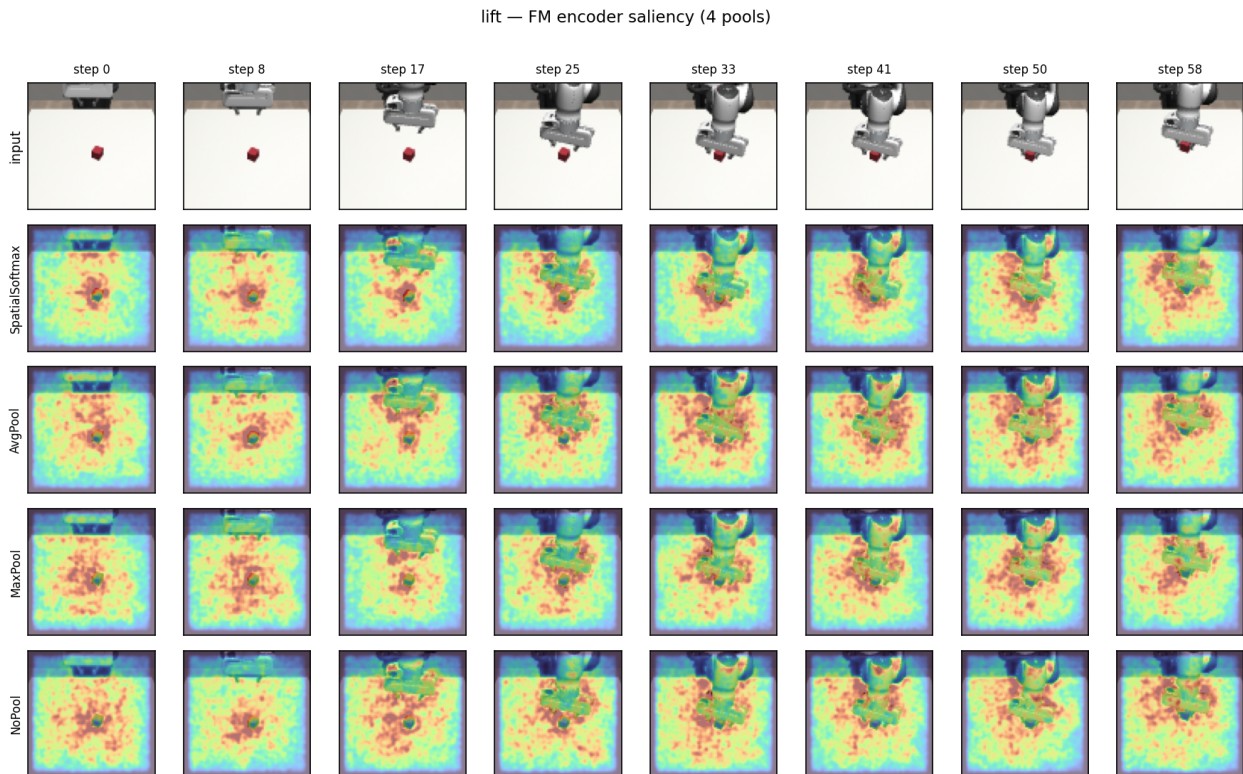


Figure 7 Saliency maps with different pooling strategies on the Lift task. SSPool-based representations tend to produce more localized saliency around the object and gripper than feature-value aggregation.

can — FM encoder saliency (4 pools)

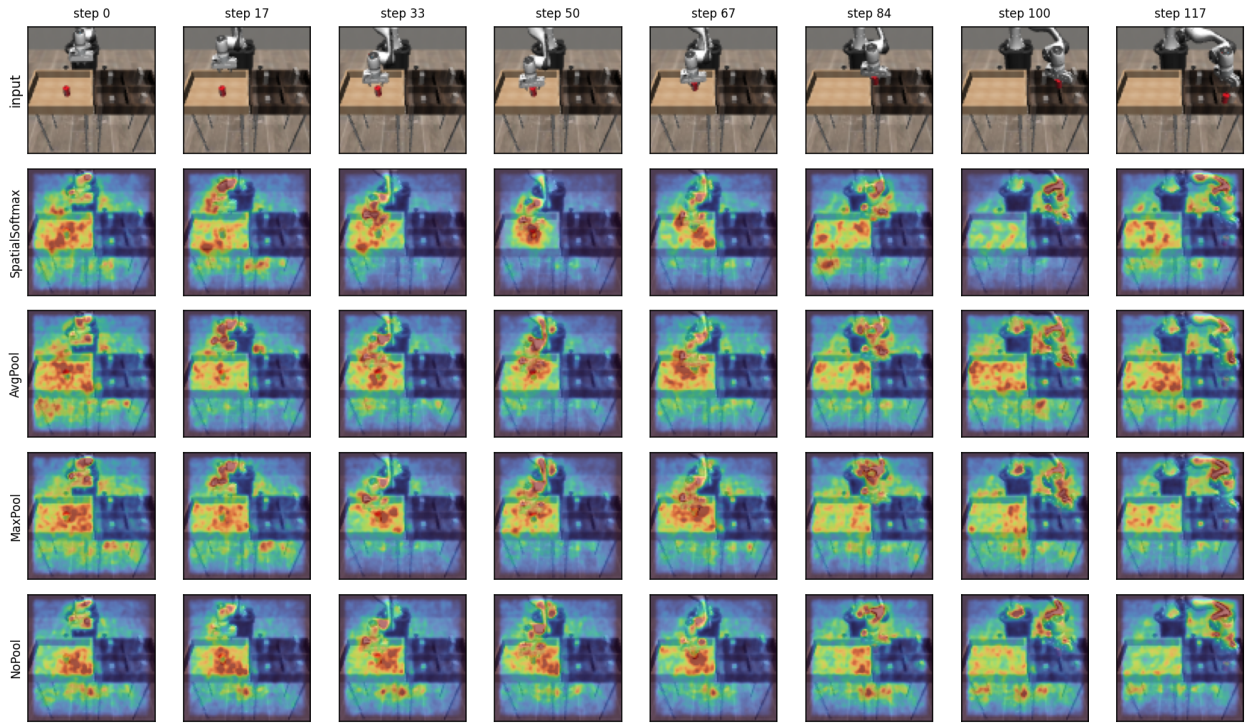


Figure 8 Saliency maps with different pooling strategies on the Can task. SSPool-based representations show more consistent focus on task-relevant object and interaction regions.

A.2 Realworld and Multi-Task Evaluation on LIBERO

We provide additional visualizations of the evaluation settings used in our experiments. Fig. 11 shows the LIBERO-10 benchmark tasks, which cover diverse long-horizon manipulation scenarios involving object rearrangement, articulated object interaction, and multi-step instruction following. Fig. 12 shows the LIBERO-Spatial tasks, which emphasize spatial reasoning and object arrangement under language-conditioned manipulation. These tasks provide complementary evaluation settings to Robomimic, allowing us to examine whether preserving implicit spatial representations remains useful beyond the single-task imitation learning setting.

We also visualize the real-world experimental setup in Fig. 13. The real-world experiments are conducted with a Franka Panda robot under image-based policy control. The setup includes tabletop manipulation tasks that require accurate object localization, robot-object alignment, and contact-aware motion. These real-world evaluations provide a practical test of whether the proposed representation design can support spatially precise manipulation beyond simulation.

square — FM encoder saliency (4 pools)

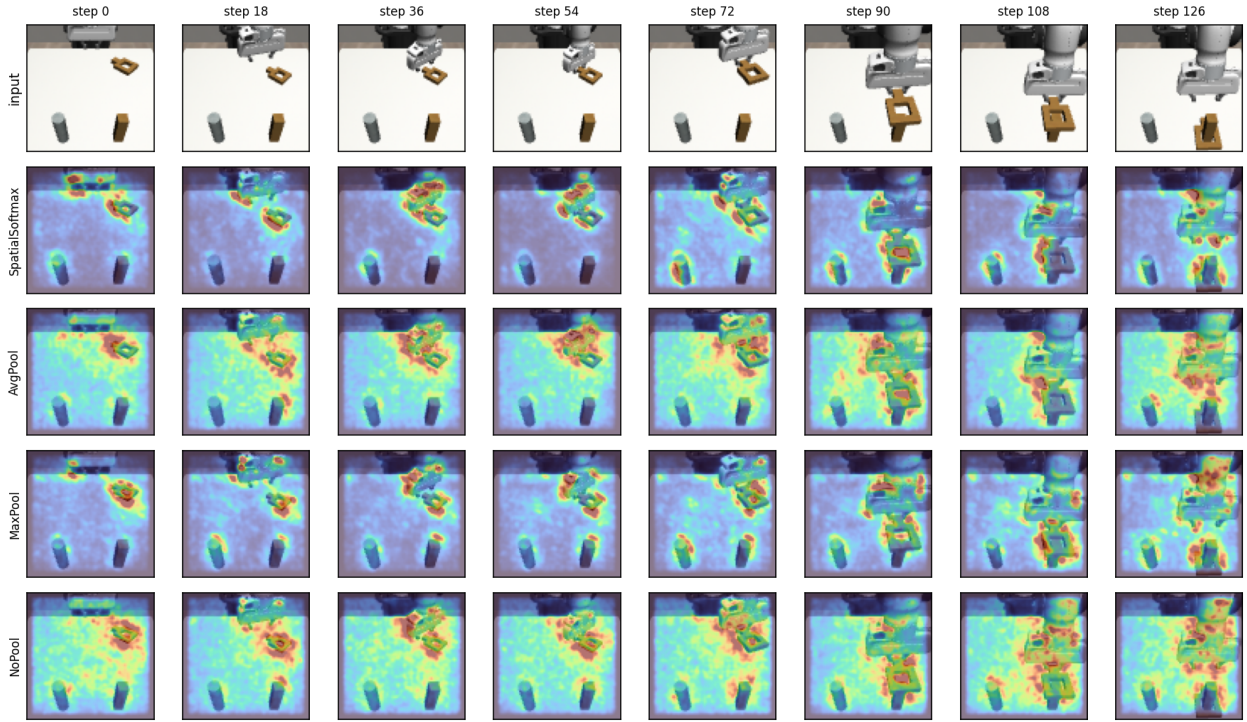


Figure 9 Saliency maps with different pooling strategies on the Square task. SSPool-based representations better preserve spatially localized cues needed for object alignment and placement.

A.3 Training Details

All three baselines (DDPM-UNet, FM-UNet, and MeanFlow-UNet) share the same observation encoder, UNet backbone, optimizer, and dataloader configuration, differing only in their noise model and method-specific hyperparameters. All experiments use batch size 512, trained for 200 epochs on Robomimic with image observations of shape $3 \times 84 \times 84$. The following tables document all hyperparameters required to reproduce our results.

A.3.1 Shared Training Configuration

All methods are trained with AdamW under a cosine learning rate schedule with a linear warmup period. The encoder is trained end-to-end jointly with the policy network without any frozen layers. Table 8 summarises the optimisation hyperparameters, and Table 9 lists the temporal horizon settings shared across all policies.

A.3.2 Shared Observation Encoder

All methods use a `MultiImageObsEncoder` that processes each camera view independently through a ResNet-18 backbone initialised from scratch (no ImageNet pretraining). BatchNorm layers are replaced by GroupNorm to improve stability under the small effective per-device batch sizes that arise with image observations. Random cropping and ImageNet-style mean/std normalisation are applied as data augmentation during training. Camera-specific weights are *not* shared, allowing the encoder to specialise to each viewpoint. The full configuration is given in Table 10.

A.3.3 Shared 1D Conditional UNet

The denoising backbone is a 1D temporal UNet that conditions on the encoded observation via FiLM-style modulation (`cond_predict_scale=True`). The network operates on action sequences of length $H = 16$ and

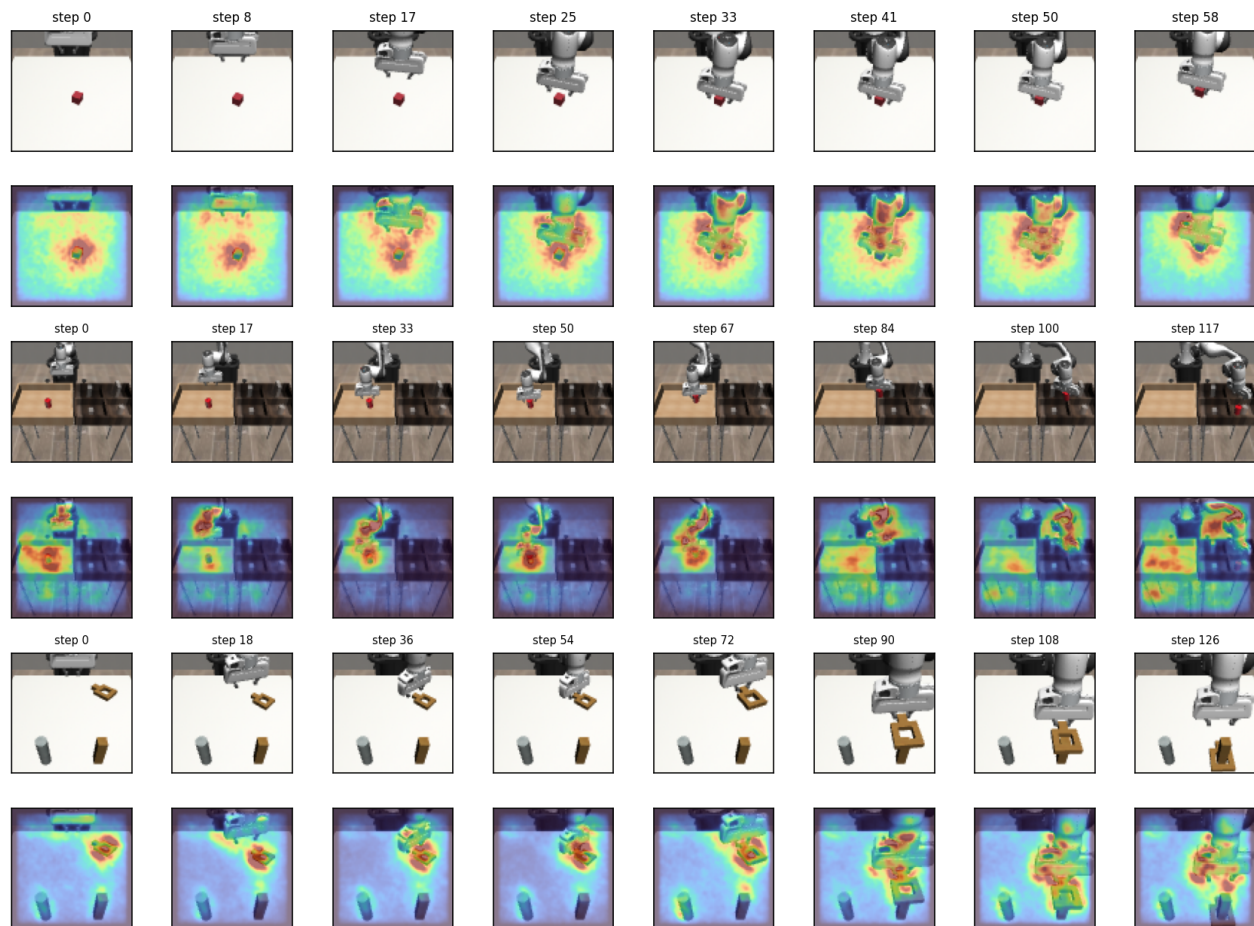


Figure 10 Saliency maps of PRISM on the Lift, Can, and Square tasks. PRISM focuses on task-relevant regions, including the manipulated object, the gripper, and robot-object interaction areas.

LIBERO-10 tasks

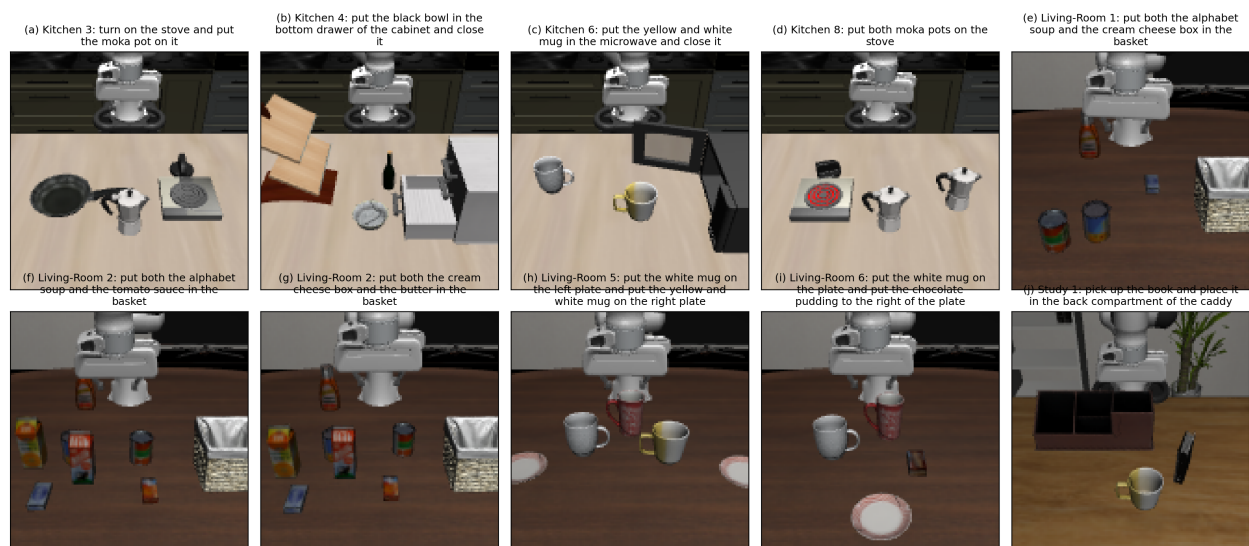


Figure 11 Visualization of the LIBERO-10 benchmark tasks. LIBERO-10 contains diverse long-horizon manipulation tasks involving object rearrangement, articulated object interaction, and multi-step language-conditioned control.

LIBERO-Spatial tasks

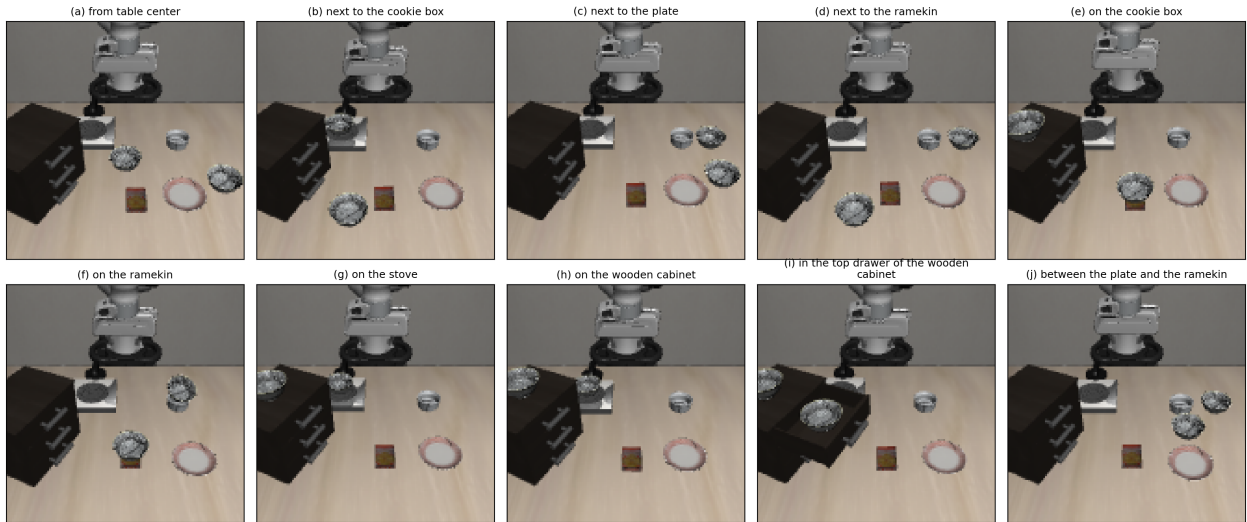


Figure 12 Visualization of the LIBERO-Spatial benchmark tasks. LIBERO-Spatial emphasizes spatial reasoning and object arrangement, providing an additional evaluation setting for spatially sensitive manipulation.

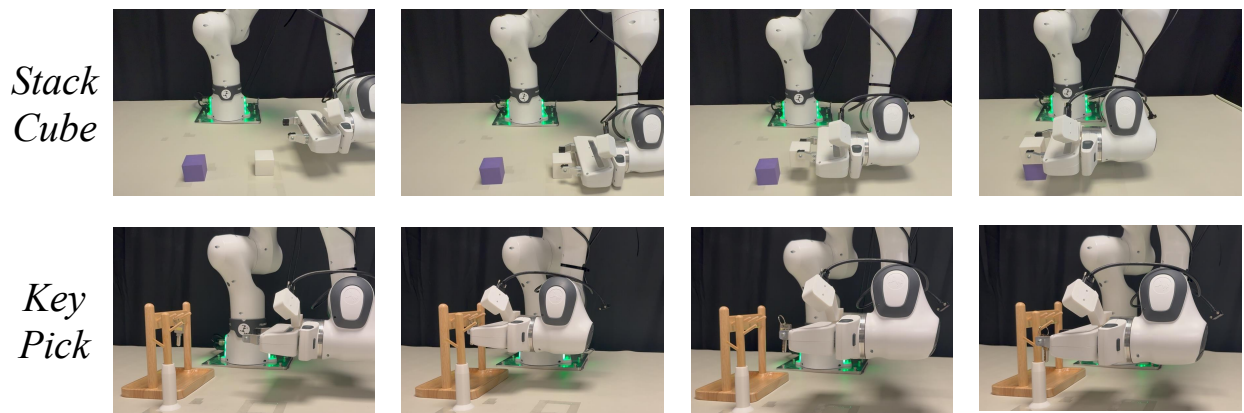


Figure 13 Real-world experimental setup. We evaluate the policy on a Franka Panda robot in tabletop manipulation settings that require object localization, robot-object alignment, and contact-aware control.

Hyperparameter	Value
Batch size (train / val)	512
Number of epochs	200
Steps per epoch	250
Gradient accumulation	1
Optimizer	AdamW
Learning rate	1×10^{-4}
Betas	(0.9, 0.999)
Epsilon	1×10^{-8}
Weight decay	1×10^{-6}
LR schedule	Cosine
LR warmup steps	500
Encoder	Trained end-to-end (not frozen)
Rollout / checkpoint interval	50 epochs

Table 8 Shared optimisation hyperparameters used across all methods.

Hyperparameter	Value
Prediction horizon H	16
Observation steps T_o	2
Action steps T_a	8
Image shape	$3 \times 84 \times 84$

Table 9 Shared runner configuration. H denotes the total prediction horizon; T_o and T_a are the number of observation context frames and executed action steps per rollout cycle, respectively.

uses three resolution levels with channel widths [256, 512, 1024]. Diffusion timestep embeddings of dimension 128 are injected at each resolution level. This backbone is shared identically across DDPM-UNet, FM-UNet, and MeanFlow-UNet; all three methods therefore have the same parameter count and receptive field. The configuration is listed in Table 11.

A.3.4 Method-Specific Hyperparameters

While the backbone and training recipe are shared, each method introduces its own noise process and inference procedure. Table 12 summarises these differences. DDPM-UNet follows the standard DDPM formulation with a squared cosine schedule and ϵ -prediction. FM-UNet uses a flow matching objective with a straight-path probability flow and requires 10 Euler steps at inference. MeanFlow-UNet replaces the multi-step ODE solver with a single-step mean-flow estimator, trading a richer training recipe (logit-normal time sampling, adaptive loss weighting, EMA) for zero-shot one-step inference.

Hyperparameter	Value
Encoder	MultiImageObsEncoder
RGB backbone	ResNet-18 (random init, no pretraining)
Normalization	GroupNorm (BatchNorm replaced)
Random crop	Enabled
ImageNet normalization	Enabled
Share RGB model across cameras	False

Table 10 Shared observation encoder configuration. GroupNorm is used in place of BatchNorm throughout the ResNet-18 backbone.

Hyperparameter	Value
Diffusion-step embedding dim	128
Down channels	[256, 512, 1024]
Kernel size	5
Group-norm groups	8
cond_predict_scale	True

Table 11 Shared 1D conditional UNet backbone used by all three methods. The same architecture serves as the denoising network (DDPM-UNet), velocity network (FM-UNet), and mean-flow network (MeanFlow-UNet).

A.4 Training Objective

This appendix details the per-sample training objectives of the three baselines used in our experiments. All three policies share the same observation encoder and 1D conditional UNet backbone, so the descriptions below isolate the generative objective itself.

Notation. Let $\tau \in \mathbb{R}^{H \times d_a}$ denote a normalized action chunk of horizon H , and let $c = \text{Enc}_\psi(\mathbf{o}_{1:T_o})$ denote the global condition produced by the observation encoder from the past T_o observation frames. Each policy parameterizes a UNet $f_\theta(\cdot, \cdot, c)$ that operates on action chunks; we use M to denote the action loss-mask (complement of the inpainting / conditioning mask). Expectations $\mathbb{E}[\cdot]$ are taken over the data distribution of (τ, c) and over all stochastic variables introduced within each objective.

A.5 Denoising Diffusion (DDPM) Policy

We adopt the standard ϵ -prediction DDPM formulation (Ho et al., 2020) with $K = 100$ training timesteps and a squared-cosine $\bar{\alpha}$ schedule. For each sample, a diffusion step $k \sim \mathcal{U}\{0, \dots, K - 1\}$ and a Gaussian perturbation $\epsilon \sim \mathcal{N}(\mathbf{0}, \mathbf{I})$ are drawn, and the noisy trajectory is constructed as

$$\tau_k = \sqrt{\bar{\alpha}_k} \tau + \sqrt{1 - \bar{\alpha}_k} \epsilon. \quad (4)$$

The network is trained to predict the injected noise by minimizing the masked mean-squared error

$$\mathcal{L}_{\text{DDPM}}(\theta, \psi) = \mathbb{E} \left[\left\| M \odot (\epsilon_\theta(\tau_k, k, c) - \epsilon) \right\|_2^2 \right]. \quad (5)$$

At inference, action chunks are generated by running the DDPM ancestral sampler for $K = 100$ denoising steps using exponential-moving-average (EMA) weights of θ and ψ .

A.6 Flow Matching (FM) Policy

We adopt conditional flow matching (Lipman et al., 2023; Liu et al., 2023b) along a straight (rectified) probability path between a Gaussian prior and the data distribution. For each sample, a prior point $x_0 \sim \mathcal{N}(\mathbf{0}, \mathbf{I})$ and a time $t \sim \mathcal{U}(0, 1)$ are drawn, yielding the interpolant

$$x_t = (1 - t)x_0 + t\tau, \quad u^*(x_t | \tau, x_0) = \tau - x_0, \quad (6)$$

Hyperparameter	Value
Noise scheduler	DDPMScheduler
β start	1×10^{-4}
β end	2×10^{-2}
β schedule	squaredcos_cap_v2
Variance type	fixed_small
Train timesteps	100
Inference steps	100
Prediction type	ϵ
clip_sample	True

(a) DDPM-UNet

Hyperparameter	Value
Inference steps	10

(b) FM-UNet

Hyperparameter	Value
Noise scheduler	DDPMScheduler (train timesteps = 100)
β start / end	$1 \times 10^{-4} / 2 \times 10^{-2}$
β schedule	squaredcos_cap_v2
Adaptive-weight norm power p	0.75
Adaptive-weight ϵ	1×10^{-3}
EDM augmentation	Disabled
EMA decay	0.9999
Time sampler	v1 (logit-normal)
$P_{\text{mean}}^t, P_{\text{std}}^t$	-0.6, 1.6
$P_{\text{mean}}^r, P_{\text{std}}^r$	-4.0, 1.6
$t=r$ sampling ratio	0.75
Inference	One-step

(c) MeanFlow-UNet

Table 12 Method-specific hyperparameter configurations. **(a)** DDPM-UNet uses a squared-cosine noise schedule with ϵ -prediction and 100 DDPM sampling steps. **(b)** FM-UNet uses a flow matching loss with straight probability paths and 10 Euler integration steps at inference. **(c)** MeanFlow-UNet trains a mean-flow estimator with logit-normal time sampling and adaptive loss weighting, enabling single-step inference at test time.

where u^* is the constant ground-truth velocity of the straight path. The network $v_\theta(x_t, t, c)$ regresses this velocity under the masked squared loss

$$\mathcal{L}_{\text{FM}}(\theta, \psi) = \mathbb{E} \left[\left\| M \odot (v_\theta(x_t, t, c) - (\tau - x_0)) \right\|_2^2 \right]. \quad (7)$$

Action chunks are obtained at inference by Euler-integrating $\dot{x}_t = v_\theta(x_t, t, c)$ from $x_0 \sim \mathcal{N}(\mathbf{0}, \mathbf{I})$ at $t = 0$ to $x_1 = \tau$ at $t = 1$ in 10 uniform steps with EMA weights. Throughout this paper the auxiliary state-consistency terms exposed by the implementation are disabled ($w_{\text{FM}} = 1$ and all auxiliary weights are zero).

A.7 MeanFlow Policy

MeanFlow (Geng et al., 2026) learns the *average* velocity field of the same straight probability path between two times $r \leq t$, so that an arbitrary flow segment can be traversed in a single network evaluation. Defining

$$\bar{u}^*(z, r, t) = \frac{1}{t-r} \int_r^t u^*(z_s, s) ds, \quad (8)$$

the average velocity satisfies the MeanFlow identity

$$\bar{u}^*(z, r, t) = u^*(z, t) - (t-r) \frac{d}{dt} \bar{u}^*(z, r, t), \quad (9)$$

which provides a self-consistent regression target without requiring numerical integration. We parameterize the average velocity as $u_\theta(z, t, h, c)$ with $h = t - r$ and train it using a single network call together with one Jacobian-vector product (JVP), as follows.

For each sample, an independent Gaussian perturbation $e \sim \mathcal{N}(\mathbf{0}, \mathbf{I})$ and a pair of times (t, r) are drawn. The two times are sampled from independent logit-normal distributions (parameters $P_{\text{mean}}^t = -0.6$, $P_{\text{std}}^t = 1.6$, $P_{\text{mean}}^r = -4.0$, $P_{\text{std}}^r = 1.6$), and with probability 0.75 we set $r = t$ to bias training toward the instantaneous-velocity boundary case. The interpolant and instantaneous velocity along the straight path are

$$z = (1-t)\tau + te, \quad v = e - \tau. \quad (10)$$

The total derivative of u_θ along the path is then computed by a JVP along the tangent $(\dot{z}, \dot{t}, \dot{r}) = (v, 1, 0)$:

$$(u_{\text{pred}}, \dot{u}_\theta) = \text{JVP}(u_\theta; (z, t, r), (v, 1, 0)). \quad (11)$$

Substituting into (9) yields the stop-gradient regression target

$$u_{\text{tgt}} = \text{sg}[v - (t-r)\dot{u}_\theta]. \quad (12)$$

We train with the adaptive L_2 loss proposed by Geng et al. (2026): with $\Delta = \|u_{\text{pred}} - u_{\text{tgt}}\|_2^2$,

$$\mathcal{L}_{\text{MF}}(\theta, \psi) = \mathbb{E} \left[\frac{\Delta}{(\text{sg}[\Delta] + \varepsilon)^p} \right], \quad p = 0.75, \quad \varepsilon = 10^{-3}, \quad (13)$$

which down-weights large residuals and stabilizes the JVP-based target. At inference, a single forward pass with $t = 1$ and $r = 0$ produces the action chunk $\tau = z - u_\theta(z, 1, 1, c)$ from $z \sim \mathcal{N}(\mathbf{0}, \mathbf{I})$, i.e. one-step generation. EMA weights of decay 0.9999 are used during evaluation.